



Cite this: DOI: 10.1039/c4dt02127d

Facile fabrication of heterostructured g-C₃N₄/Bi₂MoO₆ microspheres with highly efficient activity under visible light irradiation †

Tao Yan,^{a,b} Qing Yan,^b Xiaodong Wang,^c Hongye Liu,^c Mengmeng Li,^c Shixiang Lu,^a Wenguo Xu^{*a} and Meng Sun^{*b}

A facile and template-free solvothermal method was developed for the synthesis of microspheric g-C₃N₄/Bi₂MoO₆ photocatalysts. The obtained g-C₃N₄/Bi₂MoO₆ composites were characterized using X-ray diffraction (XRD), Fourier transform infrared spectroscopy (FT-IR), X-ray photo-electron spectroscopy (XPS), scanning electron microscopy (SEM), transmission electron microscopy (TEM), high-resolution transmission electron microscopy (HRTEM), and ultraviolet-visible diffuse reflection spectroscopy (DRS). The XRD, FTIR, and HRTEM characterization results confirmed the formation of heterojunction structures at the interfaces of g-C₃N₄ and Bi₂MoO₆. The DRS results showed that the absorption edges of g-C₃N₄/Bi₂MoO₆ composites were red shifted in the visible light region with the increase of g-C₃N₄ content. The SEM and TEM images revealed that the composites exhibited a microsphere-like morphology and were composed of smaller nanoplates. The elemental mapping images revealed that g-C₃N₄ and Bi₂MoO₆ nanoflakes uniformly assembled together to form hierarchical flowers. Compared with pure g-C₃N₄ and Bi₂MoO₆, the as-prepared samples exhibited superior photocatalytic activity towards the degradation of dyes (Rhodamine B and Methyl blue) under visible light irradiation. The enhanced photocatalytic activity of g-C₃N₄/Bi₂MoO₆ composites could be attributed to their strong visible light absorption, the high migration efficiency of photo-induced carriers, and the interfacial electronic interaction. The electrochemical impedance spectroscopy (EIS) confirmed that the interface charge separation efficiency was greatly improved by coupling g-C₃N₄ with Bi₂MoO₆. It was also confirmed that the photo-degradation of dye molecules is mainly attributed to the oxidizing ability of the generated holes (h⁺) and partly to the oxidizing ability of ·O₂⁻ and ·OH radicals.

Received 5th August 2014,
Accepted 10th November 2014
DOI: 10.1039/c4dt02127d

www.rsc.org/dalton

Introduction

Since Fujishima and Honda reported the photo-electrochemical water splitting over TiO₂, a lot of research has been devoted to the development of photocatalysts. The photocatalysis tech-

nique appears to be a very promising strategy for the remediation of global air and water pollution without any secondary pollution, but using the clean solar energy.^{1–3} TiO₂ has been widely used and investigated for the photo-degradation of organic pollutants in water owing to its low cost, strong oxidation power, and non-toxicity.^{4,5} However, due to its large band gap (3.2 eV for anatase TiO₂), pure TiO₂ can absorb only a small fraction of solar energy.⁶ To fully utilize solar energy and meet the requirements of environmental pollutant treatment, a great deal of efforts has been made to develop other heterogeneous visible light photocatalysts.

Ternary bismuth oxide compounds Bi-M-O (M = Mo, W, V, Nb or Ta) with the Aurivillius structure possess unique layered structures sandwiched between perovskite polyhedra and (Bi₂O₂)²⁺ layers.^{7–9} Recently, a number of ternary bismuth oxide compounds have been used as visible light photocatalysts for environmental treatment and/or water splitting, for example, BiVO₄,¹⁰ BiTaO₄,¹¹ BiNbO₄,¹² Bi₂WO₆,^{13,14} and Bi₂MoO₆.^{15,16} As a novel photocatalyst, Bi₂MoO₆ has attracted considerable attention over the past few years. To improve the

^aSchool of Chemistry, Beijing Institute of Technology, Beijing 100081, P.R. China. E-mail: xuwgujn@163.com; Fax: +86 10 68912631; Tel: +86 10 68913125

^bSchool of Resources and Environment, University of Jinan, Shandong Provincial Engineering Technology Research Center for Ecological Carbon Sink and Capture Utilization, Jinan 250022, P.R. China. E-mail: smlcu@163.com;

Fax: +86 531 82765969; Tel: +86 531 82769235

^cSchool of Civil Engineering and Architecture, University of Jinan, Jinan 250022, P.R. China

† Electronic supplementary information (ESI) available: The typical EDX line scanning results, TG analysis for the samples, photocatalytic degradation of RhB under visible light irradiation (λ = 550 ± 15 nm), kinetics of photo-degradation of MB, time-dependent optical absorption spectra of photo-degradation of MB, photocatalytic degradation efficiency of a fixed RhB concentration (0.02 mM) for different initial dosages of CNBM-40, and plots of the reaction rate constant (k_{app}) of photo-generated carriers trapping in the system of photo-catalytic degradation of RhB. See DOI: 10.1039/c4dt02127d

photocatalytic activity of Bi_2MoO_6 for dye degradation, a variety of Bi_2MoO_6 -based composites such as $\text{Bi}_2\text{MoO}_6/\text{TiO}_2$, $\text{Bi}_2\text{MoO}_6/\text{C}$, and $\text{Ag}/\text{Bi}_2\text{MoO}_6$ has been prepared as visible light photocatalysts.^{17–19}

Recently, graphitic carbon nitride ($\text{g-C}_3\text{N}_4$) has drawn much attention due to its remarkable properties. It is a metal-free polymeric photocatalyst first reported by Wang *et al.*²⁰ The high thermal/chemical stability and desirable band gap (2.69 eV) of $\text{g-C}_3\text{N}_4$ make it a very promising organic semiconductor photocatalyst for solar energy utilization.²¹ Moreover, the preparation process was very simple and the precursor was not expensive; thereby $\text{g-C}_3\text{N}_4$ has attracted a great deal of scientific interest, especially for its applications in photo-splitting of water^{22–25} and degradation of organic pollutants.^{26–28} In the past few years, $\text{g-C}_3\text{N}_4$ has also been used to couple with other materials to prepare novel catalysts, such as $\text{g-C}_3\text{N}_4/\text{ZnO}$,²⁹ $\text{g-C}_3\text{N}_4/\text{BiOX}$ ($\text{X} = \text{Br}, \text{I}$),^{30,31} $\text{g-C}_3\text{N}_4/\text{Fe}_2\text{O}_3$,³² $\text{AgX}/\text{g-C}_3\text{N}_4$ ($\text{X} = \text{Br}, \text{I}$),³³ and $\text{g-C}_3\text{N}_4/\text{Bi}_2\text{WO}_6$.³⁴

Herein, we first report the facile preparation of microspherical $\text{g-C}_3\text{N}_4/\text{Bi}_2\text{MoO}_6$ composites, which exhibit excellent photocatalytic activity towards the degradation of dyes (such as Rhodamine B and Methyl blue) under visible light ($\lambda > 420 \text{ nm}$) irradiation. It is postulated that the excellent photocatalytic activity of $\text{g-C}_3\text{N}_4/\text{Bi}_2\text{MoO}_6$ should be ascribed to its strong visible light absorption, the high migration efficiency of photo-induced carriers, and the interfacial electronic interaction between Bi_2MoO_6 and $\text{g-C}_3\text{N}_4$. These results also provide insight into the synthesis of other composite photocatalysts.

Experimental section

Synthesis of $\text{g-C}_3\text{N}_4$ powder

All the reagents are of analytical grade and were purchased from Sino Pharm Chemical Reagent Co., Ltd. The $\text{g-C}_3\text{N}_4$ powder was synthesized by heating melamine in a muffle furnace according to the literature but with small modifications.^{35,36} Briefly, 5 g of melamine was put into a semi-closed alumina crucible with a cover. The crucible was then placed in a muffle furnace and heated to 500 °C at a heating rate of 5 °C min^{-1} , and was held for 4 h at this temperature. After the reaction, the alumina crucible was cooled to room temperature, and the products were collected and ground into powder.

Preparation of microspherical $\text{g-C}_3\text{N}_4/\text{Bi}_2\text{MoO}_6$ composites

The $\text{g-C}_3\text{N}_4/\text{Bi}_2\text{MoO}_6$ samples were synthesized using a facile solvothermal method. Typically, 2 mmol of $\text{Bi}(\text{NO}_3)_3 \cdot 5\text{H}_2\text{O}$ was added to 20 mL of an ethylene glycol solution containing dissolved $(\text{NH}_4)_6\text{Mo}_7\text{O}_{24} \cdot 4\text{H}_2\text{O}$ with the equivalent molar ratio. Then, 50 mL ethanol was slowly added to the above solution, followed by stirring for 10 min. Then, an appropriate amount of $\text{g-C}_3\text{N}_4$ was added and ultrasonicated for 30 min to be completely dispersed. The mixture was then stirred at room temperature for 60 min to form a homogeneous phase. The

resulting solution was transferred into a 100 mL Teflon-lined stainless steel autoclave and kept at 160 °C for 12 h. Subsequently, the autoclave was cooled to room temperature gradually. Finally, the precipitate was centrifuged and washed with ethanol and deionized water three times. The resulting product was dried in a vacuum oven at 60 °C for 6 h. Pure Bi_2MoO_6 were fabricated through a similar procedure in the absence of $\text{g-C}_3\text{N}_4$. According to this method, $\text{g-C}_3\text{N}_4/\text{Bi}_2\text{MoO}_6$ composites with different $\text{g-C}_3\text{N}_4$ mass ratios from 10 to 60% were synthesized and named as CNBM-10, CNBM-20, CNBM-30, CNBM-40, CNBM-50, and CNBM-60, respectively. Pure $\text{g-C}_3\text{N}_4$ was named as CN while pure Bi_2MoO_6 was named as BM.

Characterization of photocatalysts

X-ray diffraction (XRD) patterns of the obtained products were recorded on a Bruker D8 Advance X-ray diffractometer under the following conditions: generator voltage = 40 kV; generator current = 40 mA; divergence slit = 1.0 mm; Cu $\text{K}\alpha$ ($\lambda = 1.5406 \text{ \AA}$); and a polyethylene holder. X-ray photo-electron spectroscopy (XPS) was used to identify the surface chemical composition and chemical states of the catalysts on a PHI5000 Versa Probe electron spectrometer using Al $\text{K}\alpha$ radiation (ULVAC-PHI, Japan). The morphologies and microstructures of the samples were examined with a Hitachi S-4800 scanning electron microscope (SEM). The transmission electron microscopy (TEM) and high-resolution transmission electron microscopy (HRTEM) images were recorded using a JEOL model JEM 2100 EX instrument at an accelerating voltage of 200 kV. A carbon-coated copper grid was used as the sample holder. Energy-dispersive X-ray (EDX) spectra were obtained using a JEOL-2100 at an accelerating voltage of 200 kV. Ultra-violet-visible diffuse reflectance spectroscopy (DRS) was performed at room temperature in the range of 200–700 nm on a UV-vis spectrophotometer (Cary 500 Scan Spectrophotometers, Varian, U.S.A.) equipped with an integrating sphere attachment. A NOVA 2000e (Quantachrome Instruments, USA) instrument was used to measure the Brunauer–Emmett–Teller (BET) surface areas of the samples at liquid nitrogen temperature (77.3 K). Thermogravimetric (TG) analyses were carried out on an SDT Q600 thermal analyzer (TA Instruments, U.S.A.) by heating from 50 to 850 °C at a rate of 10 °C min^{-1} in air. The FT-IR spectra were recorded on a Nicolet 5700 spectrophotometer using KBr pellets for samples. The photo-electrochemical experiment was conducted on a CHI 760E electrochemical workstation (CHI 760E Chenhua Instrument Company, Shanghai, China) in a conventional three-electrode configuration with a Pt wire as the counter electrode and a saturated calomel electrode as the reference.

Photocatalytic activity tests

Photocatalytic reactions were conducted in a customized reactor with a cooling-water-cycle system, and the reaction temperature of the aqueous solution was maintained at 25 °C. The visible light photocatalytic activity of $\text{g-C}_3\text{N}_4/\text{Bi}_2\text{MoO}_6$ composites was evaluated by photo-degradation of dyes in

aqueous solution using a 300 W xenon lamp (PLS-SXE300C, Beijing Perfect Light Co. Ltd, Beijing) with a cutoff filter ($\lambda > 420$ nm) as the light source. In each experiment, 100 mg of the photocatalyst was added to 100 mL dye aqueous solution (10 mg L^{-1}). Before irradiation, the suspensions were magnetically stirred in the dark for 60 min to ensure the establishment of an adsorption/desorption equilibrium between the photocatalyst and the dye. During the reaction process under visible light illumination, 3 mL of suspension was sampled at given time intervals and centrifuged to remove the photocatalyst particles. The resulting clear liquid was analyzed on a Perkin-Elmer UV-vis spectrophotometer (model: Lambda 35) to record the concentration changes of dye solutions.

Electrochemical impedance spectroscopy (EIS)

EIS measurements were performed in $2.5 \text{ mmol L}^{-1} \text{ K}_3\text{Fe}(\text{CN})_6\text{-K}_4\text{Fe}(\text{CN})_6$ (1 : 1) containing $0.1 \text{ mol L}^{-1} \text{ KCl}$ with a frequency range of 0.1–100 kHz at 0.24 V, and the amplitude of the applied sine wave potential in each case was 5 mV. A modified glassy carbon electrode (GCE, 4 mm diameter) was used as the working electrode, which has been prepared by a simple method as follows: a $\text{g-C}_3\text{N}_4$ homogeneous suspension was prepared by dispersing 5 mg $\text{g-C}_3\text{N}_4$ in 1 mL distilled water. Then, 20 μL of the slurry was dripped on the GCE and dried at 60°C for 120 min (denoted as CN/GCE). SS/GCE and CNBM-40/GCE in the same quantity were prepared using the same procedure.

Results and discussion

Structural characterization

Fig. 1 shows the XRD patterns of the $\text{g-C}_3\text{N}_4$, Bi_2MoO_6 , and $\text{g-C}_3\text{N}_4/\text{Bi}_2\text{MoO}_6$ composites with different mass ratios. As we can see, the pure $\text{g-C}_3\text{N}_4$ had two distinct diffraction peaks: the peak located at 27.40° represented the stacking of the conjugated double bonds, which was indexed to the (002) plane corresponding to d -spacing (0.336 nm) of $\text{g-C}_3\text{N}_4$ (JCPDS

87-1526), and the peak located at 13.04° was indexed to the (100) plane. These two diffraction peaks fit well with the $\text{g-C}_3\text{N}_4$ reported in the literature.³⁷ For Bi_2MoO_6 , four peaks located at 28.3 , 32.6 , 46.7 , and 55.4° have been observed, which matched well with the (1 3 1), (0 0 2), (0 6 0), and (3 3 1) crystal planes of Bi_2MoO_6 (JCPDS 84-0787). There is no trace of any impurity phase under the present resolution, indicating the high purity of the as-prepared samples. However, for the $\text{g-C}_3\text{N}_4/\text{Bi}_2\text{MoO}_6$ composites, only diffraction peaks of Bi_2MoO_6 have been observed. The main reason might be that the $\text{g-C}_3\text{N}_4$ entered the laminates of the Bi_2MoO_6 microsphere and became highly dispersed in the composites or the characteristic peaks of Bi_2MoO_6 (28.3°) and $\text{g-C}_3\text{N}_4$ (27.4°) were too close to distinguish.³⁸ The existence of $\text{g-C}_3\text{N}_4$ in the composite has been further identified using FT-IR, EDX and XPS characterization.

The morphology and nanostructures of $\text{g-C}_3\text{N}_4$, Bi_2MoO_6 , and $\text{g-C}_3\text{N}_4/\text{Bi}_2\text{MoO}_6$ composites were investigated using SEM and TEM. Fig. 2a shows the bulk structure of $\text{g-C}_3\text{N}_4$ without ultrasonic treatment, displaying an aggregated morphology although it was a flexibly shaped polymer semiconductor material. Fig. 2b shows the SEM image of Bi_2MoO_6 . It can be seen that the Bi_2MoO_6 exhibited a microsphere morphology with rough surfaces. Fig. 2c and d show the SEM images of CNBM-40 microspheres. It shows that the microspheres were composed of nanosheets several nanometers in thickness. The cross-linking of the nanosheets resulted in the formation of microspheres with rough surfaces. It could provide more active points for the adsorption of organic pollutants and help enhance the photocatalytic activity of the sample. The intimate interaction between $\text{g-C}_3\text{N}_4$ and Bi_2MoO_6 enhances the electron transfer capacity during the photocatalysis process.

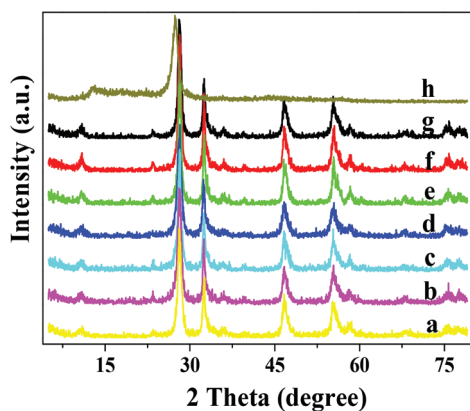


Fig. 1 XRD patterns of $\text{g-C}_3\text{N}_4/\text{Bi}_2\text{MoO}_6$ composites with different $\text{g-C}_3\text{N}_4$ contents: (a) Bi_2MoO_6 , (b) CNBM-60, (c) CNBM-50, (d) CNBM-40, (e) CNBM-30, (f) CNBM-20, (g) CNBM-10, and (h) $\text{g-C}_3\text{N}_4$.

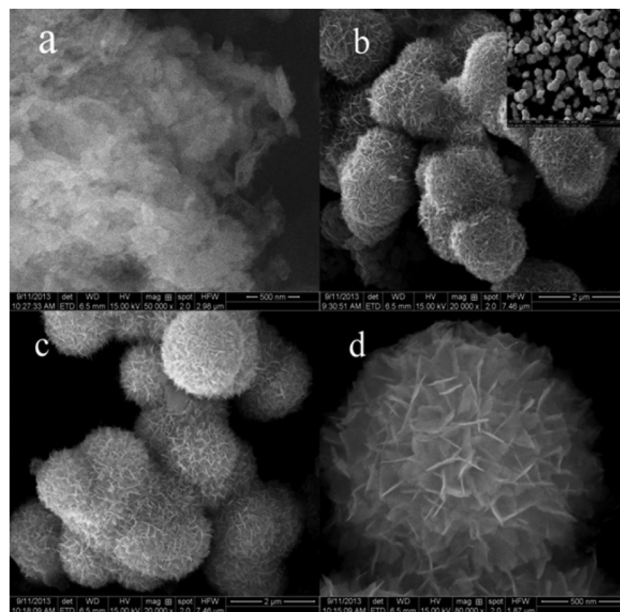


Fig. 2 SEM images of (a) $\text{g-C}_3\text{N}_4$, (b) Bi_2MoO_6 , and (c and d) low and high magnification of CNBM-40.

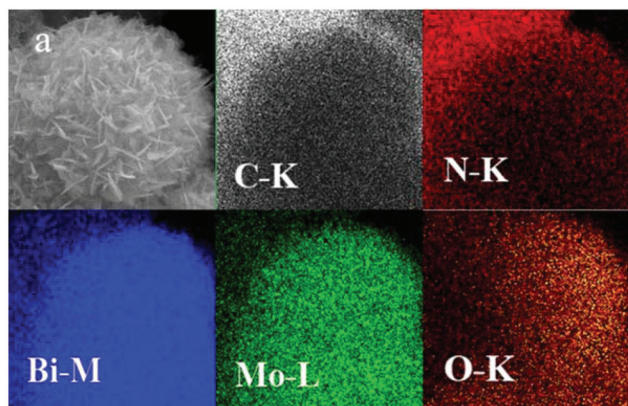


Fig. 3 SEM image of (a) CNBM-40 and corresponding elemental mapping images of the elements C, N, Bi, Mo, and O.

However, the SEM images have not enough distinguishability for analysis of the heterojunction structure.

The EDX analysis was used to track compositional homogeneity changes in the range of a few hundred nanometers to further characterize the composition and mixing quality in the interior of the microspheres. Fig. 3 displays the elemental mapping images of the sample. As can be seen, the elemental mapping images of C-K, N-K, Bi-M, Mo-L and O-K were well-defined with sharp contrast. Maps of Bi-M, Mo-L and O-K have the same shape and location, demonstrating the definite existence of Bi_2MoO_6 in the microspheres. The maps of C-K and N-K showed C and N signals, respectively, indicating the homogeneous distribution of $g\text{-C}_3\text{N}_4$ sheets on the Bi_2MoO_6 microsphere. The typical EDX line scanning results are shown in Fig. S1.† It can also be seen that the elements C, N, Bi, Mo, and O across the scanned distance are uniformly distributed. The intensity profile of various elements indicated the mixing quality, and thus demonstrated the percentage content of various elements on the surface of microspheres, which is in keeping with the above SEM results.

Fig. 4 shows the TEM images of the prepared samples. Fig. 4a shows the TEM image of $g\text{-C}_3\text{N}_4$ nanosheets with soft edges after exfoliating the bulk $g\text{-C}_3\text{N}_4$ by ultrasonic treatment. Fig. 4b shows the TEM image of the Bi_2MoO_6 microsphere. Fig. 4c and d shows the TEM and HRTEM images of the $g\text{-C}_3\text{N}_4/\text{Bi}_2\text{MoO}_6$ composite. It can be seen from Fig. 4d that the lattice structure of $g\text{-C}_3\text{N}_4$ was highly ordered, and the uniform fringe, with an interval of 0.336 nm, is in good agreement with the (002) lattice plane of $g\text{-C}_3\text{N}_4$. Another set of clear fringes with an interplanar spacing of 0.249 nm corresponds to the (151) lattice plane of Bi_2MoO_6 . These observations indicated that the $g\text{-C}_3\text{N}_4$ nanosheets are embedded in the Bi_2MoO_6 matrix. Therefore, the as-prepared composite microspheres are considered to be a strongly interacting heterostructure between $g\text{-C}_3\text{N}_4$ and Bi_2MoO_6 .

To investigate the chemical composition of the composites, FT-IR was carried out and the corresponding spectra are shown in Fig. 5. The peaks located at 842 and 796 cm^{-1} can be respectively attributed to the asymmetric and symmetric

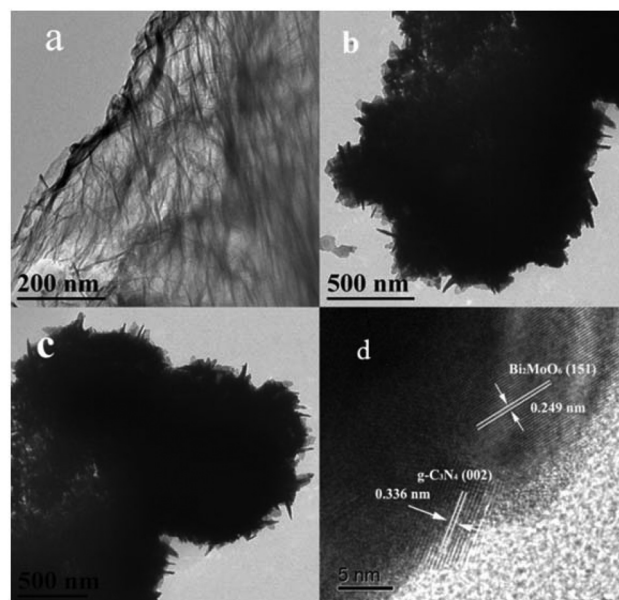


Fig. 4 TEM images of the prepared composites: (a) $g\text{-C}_3\text{N}_4$ nanosheets, (b) Bi_2MoO_6 microspheres, (c) CNBM-40 and (d) HRTEM image of CNBM-40 showing the formation of heterojunctions.

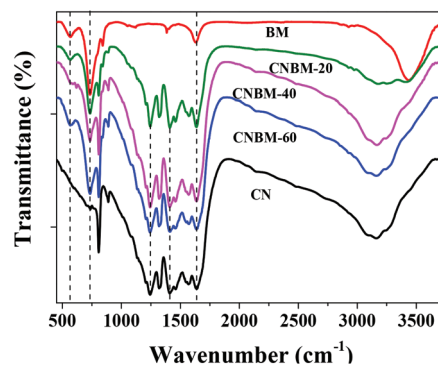


Fig. 5 FT-IR spectra of the as-synthesized samples of $g\text{-C}_3\text{N}_4$, Bi_2MoO_6 and $g\text{-C}_3\text{N}_4/\text{Bi}_2\text{MoO}_6$ composites.

vibration modes (Mo–O stretching) of the corner sharing $(\text{MoO}_6)^{6-}$ octahedron.³⁹ While the peak located at 734 cm^{-1} was assigned as the asymmetric stretching mode of MoO_6 involving vibrations of the equatorial oxygen atoms, the peak at 567 cm^{-1} corresponds to the bending vibration of the MoO_6 octahedron. The peaks at 1640 cm^{-1} were attributed to $\text{C}\equiv\text{N}$ stretching vibration modes, while those located at 1243, 1325, and 1408 cm^{-1} can be ascribed to aromatic C–N stretching vibration modes. The peak located at 808 cm^{-1} was related to the characteristic breathing mode of triazine units.⁴⁰ It could also be seen that the main characteristic peaks of $g\text{-C}_3\text{N}_4$ appeared in the $g\text{-C}_3\text{N}_4/\text{Bi}_2\text{MoO}_6$ composite which further testified the XRD results.

XPS spectra of the $g\text{-C}_3\text{N}_4/\text{Bi}_2\text{MoO}_6$ composites were presented to determine the oxidation state and elemental composition of the composites. Fig. 6a shows that the survey scan XPS spectra provided C 1s and N 1s peaks for $g\text{-C}_3\text{N}_4$ and

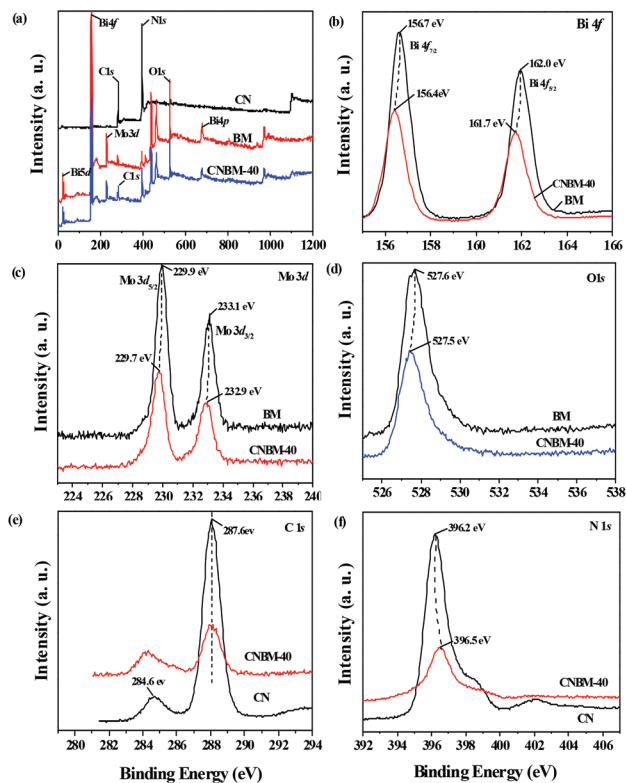


Fig. 6 XPS spectra of the as-synthesized samples: (a) the survey scan of $g\text{-C}_3\text{N}_4$, Bi_2MoO_6 and CNBM-40; (b) Bi 4f, (c) Mo 3d and (d) O 1s of Bi_2MoO_6 and CNBM-40; (e) C 1s, (f) N 1s of $g\text{-C}_3\text{N}_4$ and CNBM-40.

CNBM-40, as well as Bi 4f, Mo 3d and O 1s peaks for Bi_2MoO_6 and CNBM-40, which was consistent with the chemical composition of the photocatalysts. Fig. 6b–d depicts the high-resolution XPS spectra of Bi 4f, Mo 3d and O 1s. The characteristic spin-orbital splitting photoelectrons for Bi 4f and Mo 3d of Bi_2MoO_6 indicate a six-valent oxidation state for Mo^{6+} and Bi(III), respectively. Decreased Bi 4f, Mo 3d and O 1s peak intensities are found in the CNBM-40 compared with the Bi_2MoO_6 , deriving from the lower Bi_2MoO_6 content in the composite. The Bi 4f peaks of Bi_2MoO_6 are located at Bi $4f_{5/2}$ (156.67 eV) and Bi $4f_{7/2}$ (161.97 eV) (Fig. 6b). However, the binding energies of Bi $4f_{5/2}$ (156.41 eV) and Bi $4f_{7/2}$ (161.71 eV) of CNBM-40 were lower than those of pure Bi_2MoO_6 . A similar appearance was also found in the XPS spectra of Mo 3d (Fig. 6c) and O 1s (Fig. 6d). The binding energies of Mo $3d_{3/2}$ (229.73 eV), Mo $3d_{5/2}$ (232.87 eV) and O 1s (527.48 eV) of CNBM-40 were lower than those of Mo $3d_{3/2}$ (229.93 eV), Mo $3d_{5/2}$ (233.13 eV) and O 1s (529.1 eV) of Bi_2MoO_6 . Such results could be similarly ascribed to the interaction between $g\text{-C}_3\text{N}_4$ and Bi_2MoO_6 resulting in an inner shift of Bi 4f, Mo 3d and O 1s orbits. Fig. 6e shows high-resolution XPS spectra of $g\text{-C}_3\text{N}_4$ and CNBM-40 in the C 1s binding energy regions, and two carbon peaks at 284.6 eV and 287.6 eV were found, respectively. The first peak is attributed to the surface adventitious reference carbon.⁴¹ As for the second peak for $g\text{-C}_3\text{N}_4$ and CNBM-40 composite, it originates from carbon atoms bonded to three

nitrogen atoms in the $g\text{-C}_3\text{N}_4$ space lattice.⁴² The intensity of the C 1s peak at 287.6 eV of CNBM-40 is weakened compared with pure $g\text{-C}_3\text{N}_4$. This occurrence is also observed in the N 1s peak of CNBM-40 at 396.2 eV. The N 1s peak of $g\text{-C}_3\text{N}_4$ and CNBM-40 was observed at 396.2 eV (Fig. 6f), which arose from C=N–C coordination.²³ In addition, the binding energy of the N 1s peak of CNBM-40 was higher than that of $g\text{-C}_3\text{N}_4$. It was also due to the fact that Bi_2MoO_6 hybridized with $g\text{-C}_3\text{N}_4$ resulted in an inner shift of the N 1s orbit. TG analysis was performed to investigate the actual content of $g\text{-C}_3\text{N}_4$ in the composites. Fig. S2† shows the TG results of $g\text{-C}_3\text{N}_4$, Bi_2MoO_6 , and $g\text{-C}_3\text{N}_4/\text{Bi}_2\text{MoO}_6$ composites. The TG curve of pure $g\text{-C}_3\text{N}_4$ shows a sharp weight loss at about 700 °C, while Bi_2MoO_6 exhibits good thermal stability without any weight loss. As for the $g\text{-C}_3\text{N}_4/\text{Bi}_2\text{MoO}_6$ composites, they exhibit an obvious weight loss at a lower temperature of 520 °C. That is to say, the thermal stabilities of $g\text{-C}_3\text{N}_4/\text{Bi}_2\text{MoO}_6$ composites are lower than those that of pure $g\text{-C}_3\text{N}_4$. Fig. S2† also reveals the actual contents of $g\text{-C}_3\text{N}_4$ in the composites. It was obvious that the actual $g\text{-C}_3\text{N}_4$ contents were nearly the same as those labeled in the sample names.

Formation mechanism of the microspheric $g\text{-C}_3\text{N}_4/\text{Bi}_2\text{MoO}_6$ composites

In order to understand the formation mechanism of the hierarchical $g\text{-C}_3\text{N}_4/\text{Bi}_2\text{MoO}_6$ microspheres, time-dependent experiments were carried out while keeping the other reaction conditions constant. The samples collected at different reaction times were analyzed using SEM. As seen from Fig. 7, the reaction time has a significant effect on the composite morphology obviously. After a reaction time of 1–3 h (Fig. 7a–c), the $g\text{-C}_3\text{N}_4$ showed a mass of wrinkled sheets and the as-prepared Bi_2MoO_6 mainly presented as aggregated nanosheets depositing on the surface of $g\text{-C}_3\text{N}_4$ sheets. When the reaction time was increased to 4–7 h (Fig. 7d and e), the $g\text{-C}_3\text{N}_4/\text{Bi}_2\text{MoO}_6$ microspheres began to form, and some irregular microspheres were observed. With further prolonging the time to 8–12 h, the $g\text{-C}_3\text{N}_4$ sheets gradually disappeared, and lots of $g\text{-C}_3\text{N}_4/\text{Bi}_2\text{MoO}_6$ microspheres were obtained (Fig. 7f).

BET surface area analysis

Fig. 8 shows the nitrogen adsorption–desorption isotherms for different samples, which exhibited a type IV with a H3 hysteresis loop in the range of 0.6–1.0 P/P_0 .⁴³ The BET surface areas of the samples were calculated and are listed in Table 1. It can be seen that pure Bi_2MoO_6 showed a relatively large specific surface area (35.68 $\text{m}^2 \text{g}^{-1}$), and $g\text{-C}_3\text{N}_4$ had the lowest surface area of 8.51 $\text{m}^2 \text{g}^{-1}$. The surface areas of the $g\text{-C}_3\text{N}_4/\text{Bi}_2\text{MoO}_6$ composites slightly decreased as the mass ratio of $g\text{-C}_3\text{N}_4$ increased. The reaction rate constant k of the $g\text{-C}_3\text{N}_4/\text{Bi}_2\text{MoO}_6$ composites was also calculated. As shown in Table 1, all the normalized rate constants of $g\text{-C}_3\text{N}_4/\text{Bi}_2\text{MoO}_6$ composites were higher than those of pure Bi_2MoO_6 , indicating that the formation of heterojunctions has an important effect on improving the photocatalytic degradation activity. The specific

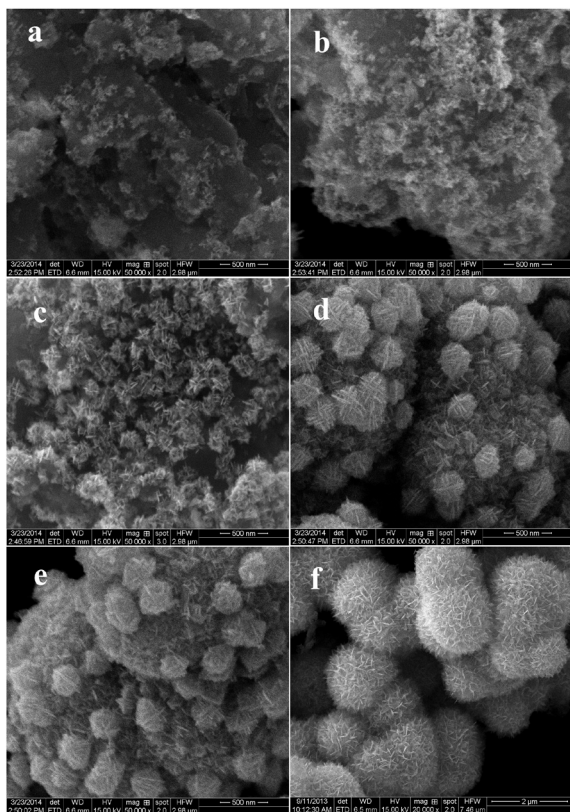


Fig. 7 SEM images of CNBM-40 obtained after different reaction times at 160 °C. (a) 1 h, (b) 3 h, (c) 5 h, (d) 7 h, (e) 9 h and (f) 12 h.

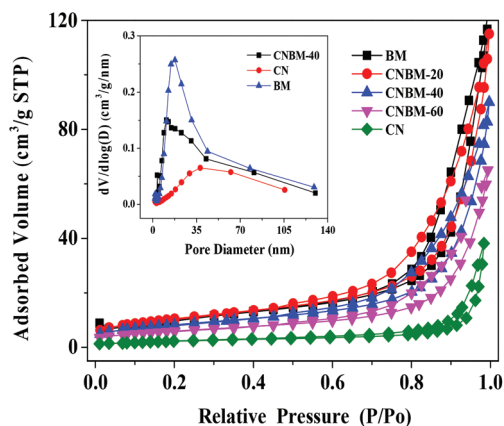


Fig. 8 Nitrogen sorption isotherm and the corresponding pore size distribution plot (inset) of the as-prepared samples.

surface area, pore volume and pore size distribution of different samples are summarized in Table 1.

Optical characterization

The optical absorption properties played a critical role in determining the photocatalytic performance of photocatalysts. The DRS spectra of pure $g\text{-C}_3\text{N}_4$, Bi_2MoO_6 , and $g\text{-C}_3\text{N}_4/\text{Bi}_2\text{MoO}_6$ composites are shown in Fig. 9. As we can see, the light absorption abilities of the samples were different. The absorp-

Table 1 The S_{BET} values, pore volume, average pore size, and calculated reaction rate constants of different photocatalysts

Samples	S_{BET} ($\text{m}^2 \text{g}^{-1}$)	Pore volume ($\text{cm}^3 \text{g}^{-1}$)	Average pore size (nm)	Kinetic rate constant (k) (min^{-1})
Bi_2MoO_6	35.68	0.1589	17.81	0.00264
CNBM-20	34.58	0.1346	16.79	0.01219
CNBM-40	33.22	0.1177	14.17	0.06484
CNBM-60	30.17	0.0921	13.08	0.04905
$g\text{-C}_3\text{N}_4$	8.51	0.0266	12.52	0.02562

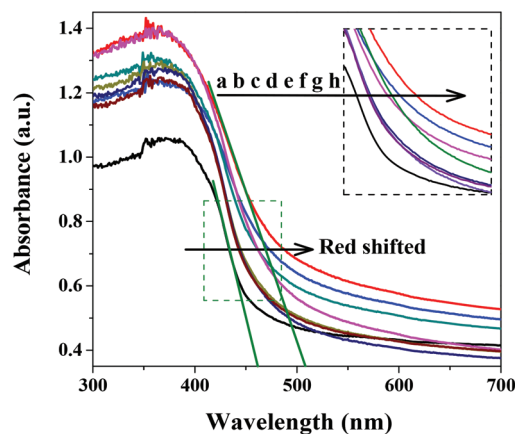


Fig. 9 UV-vis diffuse reflectance spectra of the as-prepared samples: (a) $g\text{-C}_3\text{N}_4$, (b) CNBM-60, (c) CNBM-50, (d) CNBM-40, (e) CNBM-30, (f) CNBM-20, (g) CNBM-10 and (h) Bi_2MoO_6 .

tion edge of pure $g\text{-C}_3\text{N}_4$ was estimated to be 461 nm and exhibited a strong absorption ability in the visible-light region, while that for pure Bi_2MoO_6 was located at 507 nm. It can also be clearly seen that $g\text{-C}_3\text{N}_4/\text{Bi}_2\text{MoO}_6$ composites with different $g\text{-C}_3\text{N}_4$ contents showed different absorption abilities compared with pure Bi_2MoO_6 . The absorption edges of $g\text{-C}_3\text{N}_4/\text{Bi}_2\text{MoO}_6$ composites were gradually red shifted with increasing the amount of $g\text{-C}_3\text{N}_4$ added. However, all the samples exhibited a good visible light absorption ability.

Photocatalytic activity

The visible light activities of the $g\text{-C}_3\text{N}_4/\text{Bi}_2\text{MoO}_6$ composites were mainly investigated for the degradation of RhB. As shown in Fig. 10a, the concentration change was negligible when no catalyst was added into the system. However, when $g\text{-C}_3\text{N}_4/\text{Bi}_2\text{MoO}_6$ composites were added, the photo-degradation rate was significantly improved when compared with pure $g\text{-C}_3\text{N}_4$ and Bi_2MoO_6 , and nearly 100% of RhB could be decomposed within 90 min. It was interesting to note that the photocatalytic activities of the $g\text{-C}_3\text{N}_4/\text{Bi}_2\text{MoO}_6$ composites were first remarkably enhanced with increasing the $g\text{-C}_3\text{N}_4$ content. However, when the $g\text{-C}_3\text{N}_4$ content was larger than 40%, the photocatalytic activities would decrease gradually, suggesting that the optimal $g\text{-C}_3\text{N}_4$ mass ratio in the $g\text{-C}_3\text{N}_4/\text{Bi}_2\text{MoO}_6$ composites was 40%.

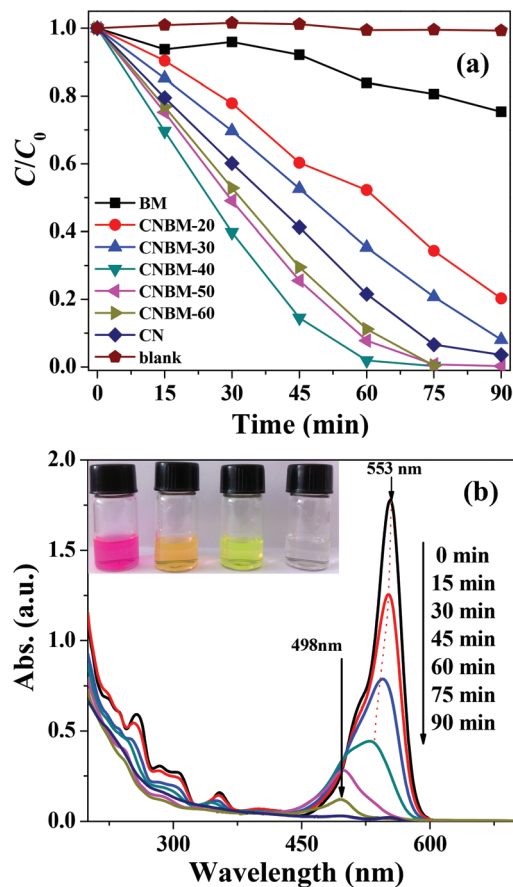


Fig. 10 (a) The kinetics of photo-degradation of RhB (0.02 mM) over different composites under visible-light ($\lambda > 420$ nm) irradiation. (b) Time-dependent optical absorption spectra of RhB over CNBM-40.

To further study the photocatalytic degradation process of RhB, the UV-vis spectra of the RhB aqueous solution at different visible light irradiation times in the presence of CNBM-40 are illustrated in Fig. 10b. It has been reported that the photo-degradation of RhB took place by two competitive processes: the destruction of the conjugated structure and N-demethylation.⁴⁴ In this degradation process, the main absorption peak of RhB gradually shifted from 553 to 498 nm, corresponding to the stepwise formation of a series of N-de-ethylated intermediates. With prolonging the reaction time, the intensity of the peak located at 498 nm would also decrease, indicating that the RhB molecules were further decomposed into smaller molecular fragments. Correspondingly, the color of the suspension changed gradually from the initial fuchsia *via* light green-yellow to colorless (Fig. 10b inset).

To investigate the reaction kinetics of RhB degradation, the degradation data were analyzed with the pseudo-first-order model, $-\ln(C/C_0) = kt$, where C is the concentration of RhB at time t , C_0 is the original concentration of RhB, and k is the reaction rate constant. It can be seen from Fig. 11 that the k of CNBM-40 (0.06484 min^{-1}) is about 2.5 times that of $g\text{-C}_3\text{N}_4$ (0.02562 min^{-1}) and is about 25 times that of Bi_2MoO_6

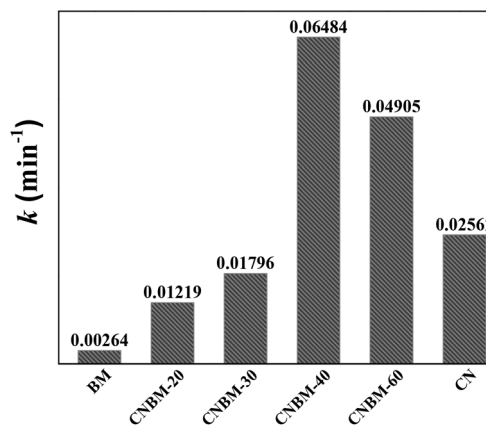


Fig. 11 The reaction rate constants of different composites for the degradation of RhB under visible light.

(0.00264 min^{-1}). From the above results, we conclude that all the $g\text{-C}_3\text{N}_4/\text{Bi}_2\text{MoO}_6$ composites exhibit much higher photocatalytic activities than those of single phase $g\text{-C}_3\text{N}_4$ or Bi_2MoO_6 . The enhancement of the photocatalytic activities of the $g\text{-C}_3\text{N}_4/\text{Bi}_2\text{MoO}_6$ composites in comparison to individual components may be due to the formation of heterojunctions between n-type Bi_2MoO_6 and p-type $g\text{-C}_3\text{N}_4$, facilitating separation of electron-hole pairs at the interface. Such a synergistic effect was also favorable for the photo-degradation of MB. As can be seen from Fig. S3† and S4, nearly 100% of MB had been decomposed within 120 min under visible light ($\lambda > 420$ nm) illumination in the presence of CNBM-40.

To investigate the influence of different initial dosages of CNBM-40 on the degradation rates, a series of experiments has been carried out to find the optimal value by varying the dosage of CNBM-40, and the results are shown in Fig. 12. As can be seen from Fig. 12 and Fig. S5†, the effect of catalyst dosage on the degradation rate was studied by varying the amount of CNBM-40 from 5 to 15 mg L^{-1} . As expected, the degradation rate of RhB first gradually increased with increasing the CNBM-40 amount, because more active sites would be

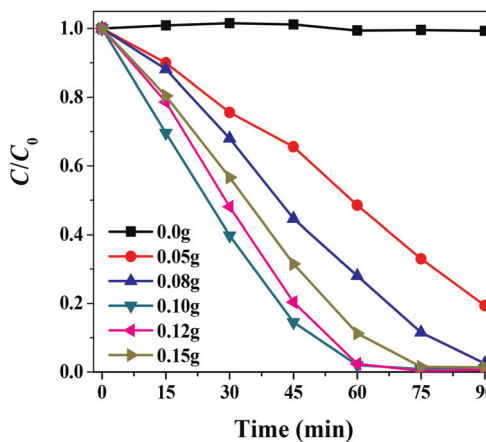


Fig. 12 Influence of the catalyst dosage on the photo-degradation rate of RhB solutions.

provided. However, when the amount was more than 12 mg L⁻¹, the degradation rate would inversely decrease because greater photocatalyst aggregation occurred. What was worse is that the scattering of light would severely reduce the light intensity penetrated through the RhB solution. In order to prove that dye sensitization was not the main reason for its high activity, visible light with a wavelength of 550 ± 15 nm has been used as the light source to investigate the degradation of RhB over CNBM-40. The degradation results are shown in Fig. S6.† It shows that the photoactivity of CNBM-40 severely decreased, and the degradation ratio was about 12% after 60 min of reaction, while that observed under visible light irradiation ($\lambda > 420$ nm) was nearly 100%. That is to say, dye sensitization only played a minor role in the degradation of RhB under visible light irradiation ($\lambda > 420$ nm).

Regeneration and reusability

From the viewpoint of practical application, it is important to evaluate the stability of the g-C₃N₄/Bi₂MoO₆ catalyst. It has been reported that Bi₂MoO₆ might change into Bi₂O₂CO₃ after visible light irradiation.⁴⁵ So, XRD patterns of the g-C₃N₄/Bi₂MoO₆ composite before and after usage were acquired and are shown in Fig. 13a. It was found that the XRD patterns of these two samples were nearly the same, indicating that the crystal structure had not changed after the photocatalytic reaction. The activity stability was also checked by repeating the photocatalytic degradation processes five times, as shown in Fig. 13b. The results indicated that the g-C₃N₄/Bi₂MoO₆ composites had high and stable activity for photocatalytic decomposition of dye in water. After five run cycles, the photocatalyst did not show any loss of activity. In this work, the g-C₃N₄/Bi₂MoO₆ catalyst could be easily separated from RhB aqueous solution by sedimentation, which was beneficial for its reuse.

Possible photocatalytic mechanism

Electrochemical impedance spectroscopy (EIS). To investigate the influence of g-C₃N₄ hybridization on photoelectric properties, the electrochemical impedance spectroscopy (EIS) technique was used to study the solid–electrolyte interfaces of Bi₂MoO₆, g-C₃N₄, and CNBM-40 samples. The results were shown in Fig. 14. As we can see, the arc radius of the EIS Nyquist plot for the CNBM-40 electrode was smaller than that of Bi₂MoO₆ and g-C₃N₄ electrodes. A smaller arc radius indicated a lower electric charge transfer resistance of the sample. Thus, in the case of CNBM-40, the photo-induced electron–hole pairs were more easily separated and transferred to the sample surface, which was due to the hybridization and interfacial interaction between g-C₃N₄ and Bi₂MoO₆.⁴⁶

Detection of active species

It is generally accepted that the photocatalytic process is induced by photo-generated electron–hole pairs. It was meaningful to identify the main active species generated in the system for investigating the photocatalytic mechanism. To estimate the influence of these reactive species on the photo-

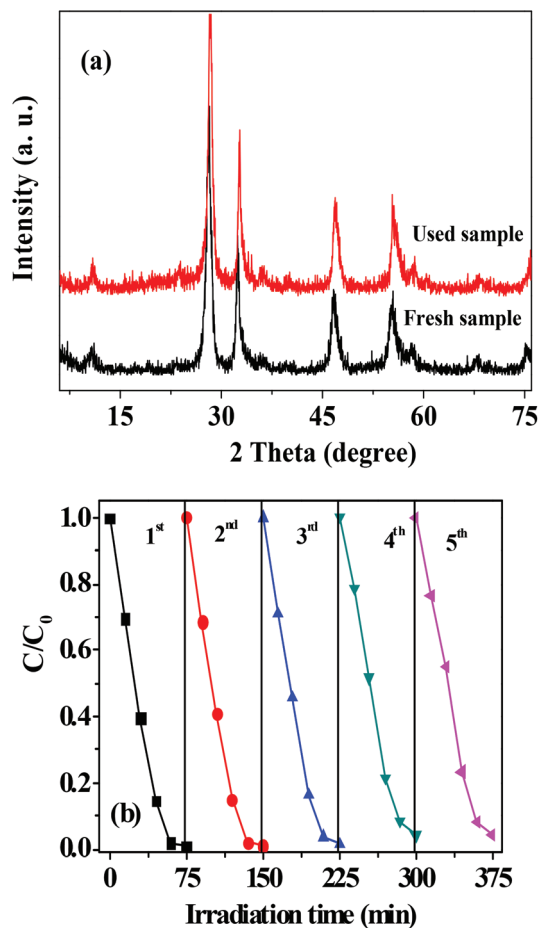


Fig. 13 (a) XRD patterns of CNBM-40 before and after photo-degradation of RhB. (b) Cycling runs of the CNBM-40 under visible light ($\lambda > 420$ nm) irradiation.

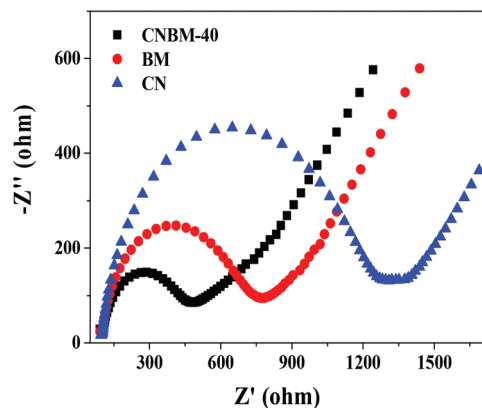


Fig. 14 EIS profiles of g-C₃N₄, Bi₂MoO₆, and CNBM-40 composite.

catalytic reactions, radical scavengers *tert*-butanol (TBA), ammonium oxalate (AO), and *p*-benzoquinone (BQ) have been, respectively, added to the degradation system. Fig. 15 shows that when 2 mL of TBA (\cdot OH scavenger) was added, the

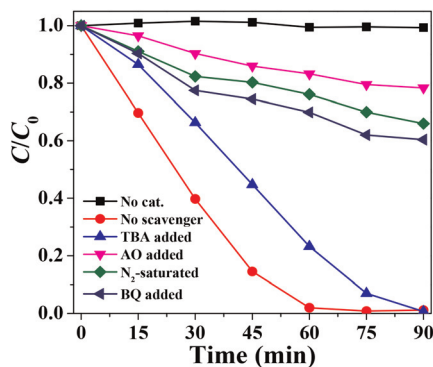


Fig. 15 Trapping experiment of active species during the photocatalytic degradation of RhB over CNBM-40 under visible light ($\lambda > 420$ nm) irradiation.

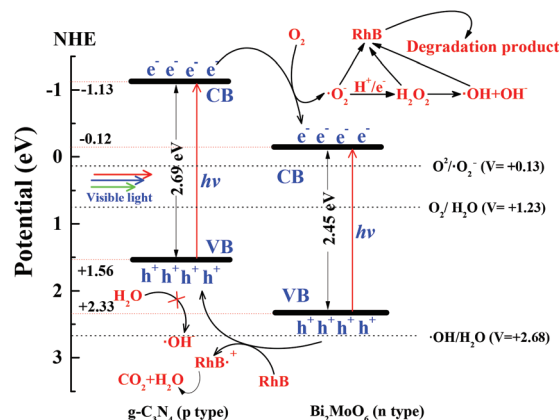
degradation rate of RhB would be decreased apparently. However, when 0.1 g of AO (h^+ scavenger) was added to the reaction system, the degradation rate was severely decreased, which meant the holes might play a more important role in the degradation process. The BQ has the ability to trap $\cdot O_2^-$ by a simple electron-transfer mechanism.⁴⁷ The addition of BQ (1.0 mg) leads to partial inhibition of the RhB degradation, and the degradation rate was largely suppressed.

Then, N_2 was bubbled through the catalytic system at the rate of 40 mL min^{-1} to ensure that the reaction was operated without O_2 as an electron scavenger to produce a variety of active oxygen species. The degradation efficiency of RhB showed an obvious decrease in comparison with the case of the air-equilibrated solution, and further indicated that $\cdot O_2^-$ played a role in the degradation of RhB. Based on the integrated analysis of the above results, we can conclude that the degradation of RhB was driven mainly by the participation of h^+ , $\cdot O_2^-$ radicals played a secondary role and $\cdot OH$ radicals to a lesser extent partook in that process (Fig. S7[†]).

The proposed photocatalytic mechanism

Based on the experimental results discussed above the mechanism for photocatalytic degradation of dyes on $g\text{-C}_3\text{N}_4/\text{Bi}_2\text{MoO}_6$ microspheres was proposed and is presented in Scheme 1. After contact, the p-n junction was formed between $g\text{-C}_3\text{N}_4$ and Bi_2MoO_6 , both of them could be excited by visible light ($\lambda > 420$ nm), and then electrons and holes were generated (eqn (1)). Due to their matching energy levels, photo-generated electrons would easily transfer from the conduction band of $g\text{-C}_3\text{N}_4$ to that of Bi_2MoO_6 . Correspondingly, the holes could facilitate transfer from the valence band of Bi_2MoO_6 to that of $g\text{-C}_3\text{N}_4$. As reported by Guo *et al.*,⁴⁸ the interfacial charge transfer could effectively enhance the separation efficiency of photo-generated electrons and holes.

The enhancement mechanism of the photocatalytic activity of the composite can be further revealed by the band edge positions of the two semiconductors. The conduction and

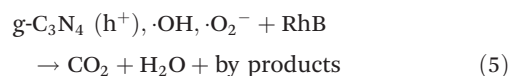
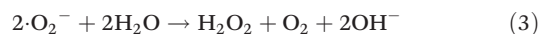
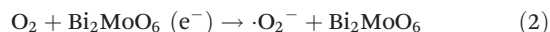
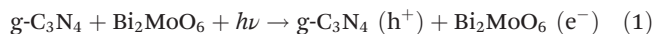


Scheme 1 Postulated mechanism of the photo-degradation of RhB over the CNBM-40 photocatalyst under visible-light ($\lambda > 420$ nm) irradiation.

valence band positions of the prepared samples were calculated through the equation:

$$E_{\text{VB}} = X - E^e + 0.5E_g$$

where X is Mulliken's electronegativity, E^e is the energy of free electrons on the hydrogen scale (4.50 eV), and E_g is the band gap.⁴⁹ Accordingly, the top of the valence band (VB) and the bottom of the conduction band (CB) of Bi_2MoO_6 were calculated to be +2.33 and -0.12 eV (*vs.* NHE), respectively. The VB and CB of $g\text{-C}_3\text{N}_4$ were estimated to be +1.56 and -1.13 eV (*vs.* NHE), respectively. The redox potential (Φ) values of the photo-generated carriers were approximately equal to those of the energy bands they stayed in.³ Hence, when the photo-generated electrons (e^-) and holes (h^+) were separated effectively under visible light ($\lambda > 420$ nm) irradiation, the photo-induced holes (h^+) could not directly oxidize the adsorbed H_2O molecules to $\cdot OH$ radicals because their potential $\Phi(h^+)$ was lower than $\Phi(\cdot OH/\text{H}_2\text{O})$ (+2.68 V), which suggests that $\cdot OH$ are likely to be formed by the reaction between the photo-induced electrons and H_2O_2 . However, the potential for $\Phi(e^-)$ was more negative than $\Phi(\text{O}_2/\cdot O_2^-)$ (+0.13 V), which allowed the yield of $\cdot O_2^-$ radicals *via* the reduction of dissolved O_2 by CB electrons (eqn (2)). After that, the yield of $\cdot OH$ from $\cdot O_2^-$ with the assistance of photo-induced electrons (e^-) has been revealed (eqn (3)–(4)). Consequently, the photo-generated holes (h^+) together with $\cdot O_2^-$ radicals and $\cdot OH$ radicals participate in the degradation of dyes (eqn (5)).



Conclusions

A novel visible light responsive g-C₃N₄/Bi₂MoO₆ composite has been successfully synthesized *via* a facile and template-free solvothermal method. The SEM and TEM analyses indicated that g-C₃N₄/Bi₂MoO₆ composites were 3D microspheres consisting of numerous nanosheets. The EDX, HRTEM and FT-IR analyses indicated that g-C₃N₄ combined and dispersed well on the Bi₂MoO₆ microspheres, which facilitated electron-hole separation, and led to the increased photo-degradation activity. Among these g-C₃N₄/Bi₂MoO₆ composites, the highest degradation efficiency was achieved for the CNBM-40 sample. The radical trap experiments showed that the degradation of RhB was driven mainly by the participation of holes (h⁺) *via* the direct holes oxidation process, and partly by the action of ·O₂⁻ and ·OH radicals. A photocatalytic mechanism has been proposed based on energy band positions of g-C₃N₄ and Bi₂MoO₆. This strategy is expected to be extended to other g-C₃N₄ loaded materials, which might have potential applications in removing pollutants.

Acknowledgements

This work was financially supported by the National Natural Science Foundation of China (no. 21271027, 21103069, and 40672158), the 863 Project of China (no. 20140AA065103-1), Scientific Research Reward Fund for Excellent Young and Middle-Aged Scientists of Shandong Province (BS2012HZ001), and Scientific Research Foundation for Doctors of University of Jinan (XBS1037, XKY1321, and XKY1043).

Notes and references

- 1 A. Fujishima and K. Honda, *Nature*, 1972, **238**, 37.
- 2 A. L. Linsebigler, G. Q. Lu and J. T. Yates, *Chem. Rev.*, 1995, **95**, 735.
- 3 M. R. Hoffmann, S. T. Martin, W. Y. Choi and D. W. Bahnemann, *Chem. Rev.*, 1995, **95**, 69.
- 4 Y. Park, S. H. Lee, S. O. Kang and W. Choi, *Chem. Commun.*, 2010, **46**, 2477.
- 5 Z. Y. Liu, X. T. Zhang, S. Nisimoto, T. Murakami and A. Fujishima, *Environ. Sci. Technol.*, 2008, **42**, 8547.
- 6 C. X. Wang, L. W. Yin, L. Y. Zhang, Y. X. Qi, N. Lun and N. N. Liu, *Langmuir*, 2010, **26**, 12841.
- 7 H. Fu, C. Pan, W. Yao and Y. F. Zhu, *J. Phys. Chem. B*, 2005, **109**, 22432.
- 8 J. W. Tang, Z. G. Zou and J. H. Ye, *Catal. Lett.*, 2004, **92**, 53.
- 9 A. Kudo, K. Omori and H. Kato, *J. Am. Chem. Soc.*, 1999, **121**, 11459.
- 10 S. Kohtani, J. Hiro, N. Yamamoto, A. Kudo, K. Tokumura and R. Nakagaki, *Catal. Commun.*, 2005, **6**, 185.
- 11 R. Shi, J. Lin, Y. J. Wang, J. Xu and Y. F. Zhu, *J. Phys. Chem. C*, 2010, **114**, 6472.
- 12 S. S. Dunkle and K. S. Suslick, *J. Phys. Chem. C*, 2009, **113**, 10341.
- 13 L. S. Zhang, H. L. Wang, Z. G. Chen, P. K. Wong and J. S. Liu, *Appl. Catal., B*, 2011, **106**, 1.
- 14 L. W. Zhang, Y. J. Wang, H. Y. Cheng, W. Q. Yao and Y. F. Zhu, *Adv. Mater.*, 2009, **21**, 1286.
- 15 G. H. Tian, Y. J. Chen, W. Zhou, K. Pan, Y. Z. Dong, C. G. Tian and H. G. Fu, *J. Mater. Chem.*, 2011, **21**, 887.
- 16 M. Shang, W. Z. Wang, J. Ren, S. M. Sun and L. Zhang, *Nanoscale*, 2011, **3**, 1474.
- 17 M. Y. Zhang, C. L. Shao, J. B. Mu, Z. Y. Zhang, Z. C. Guo, P. Zhang and Y. C. Liu, *CrystEngComm*, 2012, **14**, 605.
- 18 M. Y. Zhang, C. L. Shao, J. B. Mu, X. M. Huang, Z. Y. Zhang, Z. C. Guo, P. Zhang and Y. C. Liu, *J. Mater. Chem.*, 2012, **22**, 577.
- 19 H. G. Yu, R. Liu, X. F. Wang, P. Wang and J. G. Yu, *Appl. Catal., B*, 2012, **111–112**, 326.
- 20 X. C. Wang, K. Maeda, A. Thomas, K. Takanebe, G. Xin, J. M. Carlsson, K. Domen and M. Antonietti, *Nat. Mater.*, 2009, **8**, 76.
- 21 X. C. Wang, K. Maeda, X. F. Chen, K. Takanebe, K. Domen, Y. D. Hou, X. Z. Fu and M. Antonietti, *J. Am. Chem. Soc.*, 2009, **131**, 1680.
- 22 K. Takanebe, K. Kamata, X. Wang and M. Antonietti, *Phys. Chem. Chem. Phys.*, 2010, **12**, 13020.
- 23 Q. Xiang, J. Yu and M. Jaroniec, *J. Phys. Chem. C*, 2011, **115**, 7355.
- 24 L. Ge and C. Han, *Appl. Catal., B*, 2012, **117–118**, 268.
- 25 L. Ge, C. Han, X. Xiao and L. Guo, *Int. J. Hydrogen Energy*, 2013, **38**, 6960.
- 26 S. Ye, L. G. Qiu, Y. P. Yuan, Y. J. Zhu, J. Xia and J. F. Zhu, *J. Mater. Chem. A*, 2013, **1**, 3008.
- 27 Y. Li, H. Zhang, P. Liu, D. Wang, Y. Li and H. Zhao, *Small*, 2013, **9**, 3336.
- 28 Y. Lan, X. Qian, C. Zhao, Z. Zhang, X. Chen and Z. Li, *J. Colloid Interface Sci.*, 2013, **395**, 75.
- 29 J. X. Sun, Y. P. Yuan, L. G. Qiu, X. Jiang, A. J. Xie, Y. H. Xie and J. F. Zhu, *Dalton Trans.*, 2012, **41**, 6756.
- 30 J. Di, J. X. Xia, S. Yin, H. Xu, M. Q. He, H. M. Li, L. Xu and Y. P. Jiang, *RSC Adv.*, 2013, **3**, 19624.
- 31 J. Di, J. X. Xia, S. Yin, H. Xu, Y. G. Xu, M. Q. He and H. M. Li, *J. Mater. Chem. A*, 2014, **2**, 5340.
- 32 S. Z. Hu, R. R. Jin, G. Lu, D. Liu and J. Z. Gui, *RSC Adv.*, 2014, **4**, 24863.
- 33 L. Xu, J. X. Xia, H. Xu, J. Qian, J. Yan, L. G. Wang, K. Wang and H. M. Li, *Analyst*, 2013, **138**, 6721.
- 34 Y. J. Wang, X. J. Bai, C. S. Pan, J. He and Y. F. Zhu, *J. Mater. Chem.*, 2012, **22**, 11568.
- 35 G. Zhang, J. Zhang, M. Zhang and X. Wang, *J. Mater. Chem.*, 2012, **22**, 8083.
- 36 J. Liu, T. Zhang, Z. Wang, G. Dawson and W. Chen, *J. Mater. Chem.*, 2011, **21**, 14398.
- 37 S. C. Yan, Z. S. Li and Z. G. Zou, *Langmuir*, 2010, **26**, 3894.
- 38 H. Xu, J. Yan, Y. G. Xu, Y. H. Song, H. M. Li, J. X. Xia, C. J. Huang and H. L. Wan, *Appl. Catal., B*, 2013, **129**, 182.

- 39 L. W. Zhang, T. G. Xu, X. Zhao and Y. F. Zhu, *Appl. Catal., B*, 2010, **98**, 138.
- 40 D. L. Jiang, L. L. Chen, J. J. Zhu, M. Chen, W. D. Shi and J. M. Xie, *Dalton Trans.*, 2013, **42**, 15726.
- 41 X. Yang, Y. H. Wang, L. L. Xu, X. D. Yu and Y. H. Guo, *J. Phys. Chem. C*, 2008, **112**, 11481.
- 42 L. Ge, F. Zuo, J. K. Liu, Q. Ma, C. Wang, D. Z. Sun, L. Bartels and P. Y. Feng, *J. Phys. Chem. C*, 2012, **116**, 13708.
- 43 Y. Y. Li, J. P. Liu, X. T. Huang and G. Y. Li, *Cryst. Growth Des.*, 2007, **7**, 1350.
- 44 X. F. Hu, T. Mohamood, W. H. Ma, C. C. Chen and J. C. Zhao, *J. Phys. Chem. B*, 2006, **110**, 26012.
- 45 Z. Q. Li, X. T. Chen and Z. L. Xue, *CrystEngComm*, 2013, **15**, 498.
- 46 X. J. Bai, L. Wang and Y. F. Zhu, *ACS Catal.*, 2012, **2**, 2769.
- 47 R. Palominos, J. Freer, M. A. Mondaca and H. D. Mansilla, *J. Photochem. Photobiol., A*, 2008, **193**, 139.
- 48 S. R. Guo, D. D. Bao, S. Upadhyayula, W. Wang, A. B. Guvenc, J. R. Kyle, H. Hosseinibay, K. N. Bozhilov, V. I. Vullev, C. S. Ozkan and M. Ozkan, *Adv. Funct. Mater.*, 2013, **23**, 5199.
- 49 Y. Xu and M. A. A. Schoonen, *Am. Mineral.*, 2000, **85**, 543.